RESEARCH ARTICLE

NANO · MICRO small
www.small-journal.com

Plexcitonic Nanorattles as Highly Efficient SERS-Encoded Tags

Carla Estévez-Varela, Sara Núñez-Sánchez, Paula Piñeiro-Varela, Dorleta Jiménez de Aberasturi, Luis M. Liz-Marzán, Jorge Pérez-Juste, and Isabel Pastoriza-Santos**

Plexcitonic nanoparticles exhibit strong light-matter interactions, mediated by localized surface plasmon resonances, and thereby promise potential applications in fields such as photonics, solar cells, and sensing, among others. Herein, these light-matter interactions are investigated by UV-visible and surface-enhanced Raman scattering (SERS) spectroscopies, supported by finite-difference time-domain (FDTD) calculations. Our results reveal the importance of combining plasmonic nanomaterials and J-aggregates with near-zero-refractive index. As plexcitonic nanostructures nanorattles are employed, based on J-aggregates of the cyanine dye 5,5,6,6-tetrachloro-1,1-diethyl-3,3-bis(4-sulfobutyl)benzimidazolocarbocyanine (TDBC) and plasmonic silver-coated gold nanorods, confined within mesoporous silica shells, which facilitate the adsorption of the J-aggregates onto the metallic nanorod surface, while providing high colloidal stability. Electromagnetic simulations show that the electromagnetic field is strongly confined inside the J-aggregate layer, at wavelengths near the upper plexcitonic mode, but it is damped toward the J-aggregate/water interface at the lower plexcitonic mode. This behavior is ascribed to the sharp variation of dielectric properties of the J-aggregate shell close to the plasmon resonance, which leads to a high opposite refractive index contrast between water and the TDBC shell, at the upper and the lower plexcitonic modes. This behavior is responsible for the high SERS efficiency of the plexcitonic nanorattles under both 633 nm and 532 nm laser illumination. SERS analysis showed a detection sensitivity down to the single-nanoparticle level and, therefore, an exceptionally high average SERS intensity per particle. These findings may open new opportunities for ultrasensitive biosensing and bioimaging, as superbright and highly stable optical labels based on the strong coupling effect.

1. Introduction

Strong coupling is a specific amplification of light-matter interaction between a confined electromagnetic field and an excitonic/molecular transition.[1] Plasmonic nanoparticles (NPs) present highly confined electromagnetic fields under localized surface plasmon resonance (LSPR) excitation, and therefore are amenable to strong coupling with excitons in quantum dots,[2] simple molecules, or complex molecules such as J-aggregates.[3–5] The coherent energy exchange between the plasmon mode and the excitonic transition is an important factor contributing to the interaction. In fact, under a strong coupling regime, the energy exchange exceeds its dissipation rate and two hybrid states with different energies (lower and upper plexcitonic modes) are formed. This effect leads to the formation of a new quasiparticle, called plexciton, with properties that are different from those of the original components.[3,4,6,7] This type of interaction is of great interest in photo/electrocatalysis, photovoltaics, environmental science, and telecommunications, due to its potential for modulating the physical and chemical properties of molecules and materials.[7]

To reach the strong coupling regime between excitons and electromagnetic fields, a suitable combination of an optical cavity

C. Estévez-Varela, S. Núñez-Sánchez, L. M. Liz-Marzán, J. Pérez-Juste, I. Pastoriza-Santos
CINBIO
Universidade de Vigo
Vigo 36310, Spain
E-mail: s.nunez.sanchez@fisica.uminho.p; pastoriza@uvigo.es

The ORCID identification number(s) for the author(s) of this article can be found under https://doi.org/10.1002/smll.202306045

DOI: 10.1002/smll.202306045

S. Núñez-Sánchez
Centro de Física das Universidades do Minho e do Porto (CF-UM-UP)
Universidade do Minho
Braga 4710-057, Portugal

P. Piñeiro-Varela, D. J. de Aberasturi, L. M. Liz-Marzán
CIC biomaGUNE
Basque Research and Technology Alliance (BRTA)
Miramon Pasealekua, 194, Donostia-San Sebastián,
Gipuzkoa 20014, Spain

P. Piñeiro-Varela, D. J. de Aberasturi, L. M. Liz-Marzán
Centro de Investigación Biomédica en Red de Bioingeniería
Biomateriales y Nanomedicina (CIBER-BBN, ISCIII)
Donostia-San Sebastián, Gipuzkoa 20014, Spain

P. Piñeiro-Varela, D. J. de Aberasturi, L. M. Liz-Marzán
Ikerbasque, Basque Foundation for Science
Bilbao 48009, Spain

and an excitonic transition is required.[8,9] The quality strong-coupling figure of merit is defined by the expression Q/V, where Q and V are the quality factor and mode volume of the cavity, respectively. As single plasmonic NPs are open cavities with low-quality factors, it is necessary to combine them with molecules supporting excitonic transitions with large molecular dipole moments.[9,10] Supramolecules, such as J-aggregates, have been proven suitable candidates herefore because they show large molecular dipole moments due to exciton delocalization between their monomers, aligned in a "head-to-tail" configuration.[10] Cyanine dyes are organic molecules that can readily form J-aggregates via molecular self-assembly induced by π–π interactions and Van der Waals forces.[11]

Although strong coupling effects between J-aggregates and plasmonic NPs have been reported,[4,12,13] several issues should be overcome to obtain reliable and efficient plexcitons. First of all, efficient strategies to promote the strong interaction between plasmonic NPs and J-aggregates are still needed. The stability of the supramolecules is often extremely sensitive to medium parameters, such as pH, ionic strength, or solvent polarity.[14,15] On the other hand, the adsorption of J-aggregates on the surface of plasmonic NPs often compromises the colloidal stability of the composite particles. Additionally, the effect of capping ligands at the plasmonic nanoparticle surface on the interaction between excitons and electromagnetic fields has not been studied in detail.

Surface-enhanced Raman scattering (SERS) is a powerful technique to probe molecules adsorbed/close to a plasmonic surface.[16] The enhancement factor (EF) in SERS is usually assumed to be directly proportional to the fourth power of the local electric field enhancement (E_{loc}^4/E_0^4).[17] Therefore, a significant effort has been made to design nanostructures supporting highly intense electromagnetic enhancements (hot spots), toward achieving improved EF in SERS.[18,19] An alternative strategy involves the use of plexcitonic NPs in the strong coupling regime. In previous works, the strong coupling regime has been presented as a means to apply plexcitonic states for suppression of photo-oxidation, autofluorescence, photochemical reactions, or environmental effects (temperature, pH), resulting in Raman signal enhancement.[12,20–23] Moreover, in all these studies, the electromagnetic response of the hybrid NPs is mainly analyzed in the lower and upper plexcitonic modes.[24]

We investigated in detail the amplification of light-matter interaction occurring in colloidal plexcitonic nanorattles with strong coupling behavior. Experimental data (UV-visible and SERS spectra), supported by finite-difference time-domain (FDTD) calculations, elucidated the importance of combining plasmonic nanomaterials with J-aggregates with near-zero-index properties.[25,26] We therefore designed plexcitonic nanostructures based on entrapping J-aggregates of 5,5,6,6-tetrachloro-1,1-diethyl-3,3-bis(4-sulfobutyl)benzimidazolocarbocyanine (TDBC) inside a mesoporous SiO_2 ($mSiO_2$) capsule containing a single silver-coated gold nanorod (Au@Ag@$mSiO_2$ nanorattle). The $mSiO_2$ capsule allows us to use high dye concentrations for optimization of the strong coupling effect while maintaining colloidal stability. We further demonstrate the outstanding performance of the obtained nanorattles as SERS tags, in both liquid and solid phases, by measuring the average SERS intensity through a combination of SERS and transmission electron microscopy (TEM).[27]

2. Results and Discussion

The J-aggregate selected for the preparation of plexcitonic NPs was TDBC (Figure S1, Supporting Information), which has been used previously for strong coupling with plasmonic NPs and thus displays well-known optical properties.[28,29] As plasmonic NPs, Au@Ag@$mSiO_2$ nanorattles composed of a hollow $mSiO_2$ capsule containing a core-shell Au@Ag nanorod (NR) were selected because the $mSiO_2$ shell facilitates the formation and deposition of J-aggregates on the metal surface, while improving the colloidal stability of the resulting plexcitonic nanorattles (**Figure 1b**; Figure S2, Supporting Information). The Au@Ag@$mSiO_2$ nanorattles were prepared as previously reported,[30] through a multistep strategy involving the use of Au@Ag NRs coated with a zeolitic imidazolate framework-8 (ZIF-8) shell (Au@Ag@ZIF-8) as a sacrificial template (see Experimental Section for more details). The synthetic strategy to obtain plexcitonic nanorattles from Au@Ag@$mSiO_2$ nanorattles is depicted in Figure 1a. The process starts with the incubation of pre-made plasmonic nanorattles with TDBC in ethanol, to facilitate the diffusion of TDBC monomers through the $mSiO_2$ shell. The formation of J-aggregates is subsequently triggered by solvent exchange from ethanol to water because the TDBC self-assembles spontaneously in water.[31] Finally, removal of J-aggregates and monomers that have not been adsorbed on the metal NP surface is performed by repeated centrifugation in ethanol. As revealed by TEM analysis (Figure 1b), the resulting plexcitonic nanorattles show folds and creases (Figure S2, Supporting Information) due to the collapse of the $mSiO_2$ shell after drying in air.

For the preparation of nanorattles, Au@Ag NRs were specifically designed to hold a longitudinal LSPR mode at 586 nm, which would match the excitonic transition of TDBC J-aggregates (Figure 1c). Thus, Au@Ag NRs were 65.5 ± 6.5 nm long and 31.8 ± 1.7 nm wide (Figures S2 and S3, Supporting Information), with an overall size of Au@Ag@$mSiO_2$ nanorattles of ≈250 nm (Figure 1b; Figure S2, Supporting Information). The deposition of TDBC on the Ag@Au NR surface is evidenced by changes in the extinction spectrum of the hybrid NPs (hereafter, plexcitonic nanorattles), featuring the characteristic extinction dip at the longitudinal LSPR band, coinciding with the wavelength of the J-aggregate exciton (Figure 1c, see further details in Section S2 and Figure S4, Supporting Information). The strong coupling of the exciton of the J-aggregates with the Au@Ag NR longitudinal LSPR results in a splitting of the LSPR band into two plexcitonic resonances at 559 nm and 604 nm, which we name upper and lower plexcitonic modes, respectively. The experimentally recorded optical response matches the spectra calculated by FDTD (Figure 1d), using as model Au@Ag NRs with similar dimensions to those obtained experimentally, coated with a 1 nm thick shell of TBDC. The $mSiO_2$ shell was not included in the model because it does not significantly contribute to the optical response, dominated by Au@Ag NRs. The TDBC dielectric properties have been often modeled as Lorentzian oscillators with strengths varying from 0.05 to 0.4.[32–34] For our system, the best fitting results were obtained for a Lorentzian oscillator with a strength of 0.13 (further details in Figure S6, Supporting Information).

The stability of plexcitonic nanorattles was investigated by redispersing them in ethanol, a solvent that favors the monomeric

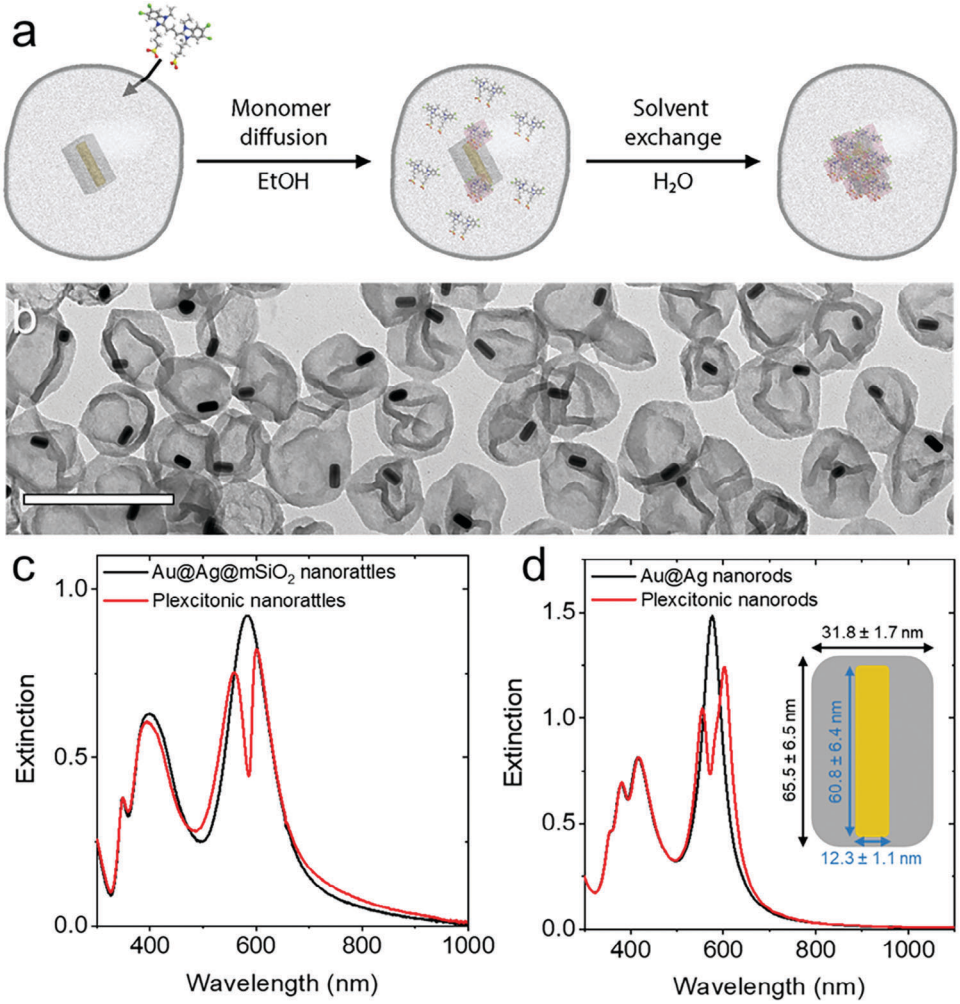

Figure 1. a) Scheme of the multistep preparation of plexcitonic nanorattles via diffusion of TDBC J-aggregates into Au@Ag@mSiO$_2$ nanorattles in ethanol, followed by solvent exchange to induce aggregation and adsorption on Au@Ag nanorods. b) Transmission electron microscopy image of plexcitonic nanorattles. Scale bar is 500 nm. c) Experimental extinction spectra of Au@Ag@mSiO$_2$ nanorattles (black) and plexcitonic nanorattles (red). d) Calculated extinction spectra of an Au@Ag NR (black) and an Au@Ag NR coated with a 1 nm thick layer of TDBC (red), with an oscillator strength of 0.13 (Figures S5 and S6, Supporting Information).

state in TDBC. As shown in Figure S7a (Supporting Information), the optical properties of plexcitonic nanorattles are not affected by the solvent, indicating colloidal stability and no J-aggregate desorption. A supplementary study was conducted with (non-coated) plexcitonic Au@Ag NRs dispersed in CTAB 10 mM. Once these particles were transferred to ethanol, the J-aggregate was found to desorb from the metal surface and colloidal stability was lost, as indicated by gradual aggregation (Figure S7b, Supporting Information).

TDBC J-aggregates are known to present Raman active vibrational modes and therefore we hypothesized that they would be suitable candidates as Raman reporters for SERS-encoded NPs (SERS tags).[35] Indeed, well-defined SERS signals ascribed to TDBC J-aggregates were obtained when the plexcitonic nanorattles were illuminated with both the 532 and 633 nm laser lines (**Figure** 2a and raw data in Figure S7c, Supporting Information). The SERS peak at 675 cm^{-1} corresponds to the out-of-plane motion of backbone hydrogens and the deformation of imidazole rings, whereas the peak at 1200 cm^{-1} can be assigned to benzene ring breathing and imidazole ring compression, the peak at 1382 cm^{-1} to the torsional movement of hydrogens about C_{12} and hydrogen flapping about C_{13} and C_{14}, and the peaks at 1596 cm^{-1} and 1611 cm^{-1} to deformations of imidazole and benzene rings (see TDBC structure in Figure S1, Supporting Information).[35] Interestingly, as SERS tags, the plexcitonic nanorattles show good stability, as evidenced by no significant changes in their SERS signal after 15 weeks of storage in ethanol (Figure S7d, Supporting Information).

Analysis of the SERS response of plexcitonic nanorattles upon excitation with the 532 and 633 nm laser lines shows a more intense SERS signal under 532 nm excitation (150 times higher than for 633 nm excitation), despite being out of resonance with TDBC (absorption peak at 587 nm). To understand this response, we compare the behavior of a bare Au@Ag NR and a plexcitonic Au@Ag NR, at both wavelengths. It should be noted that our experimental measurements involve randomly oriented NPs in

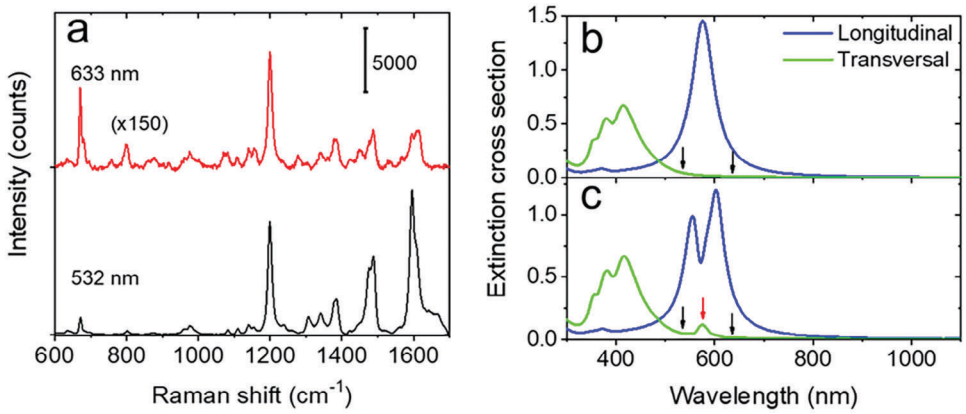

Figure 2. a) Normalized SERS spectra of the same plexcitonic nanorattles excited with the 532 nm and 633 nm laser lines. Each spectrum corresponds to the average of three measurements that were normalized by laser power and acquisition time. All SERS measurements were recorded with a 15× objective, 10 s acquisition time, and 1 accumulation. The laser power was 1.27 mW for the 532 nm laser line and 5.65 mW for the 633 nm laser line. The nanorattles concentration was 31.4 pM (1.89×10^{10} NPs mL^{-1}). b,c) Calculated extinction cross section efficiencies (normalized to the nanorod surface area) for Au@Ag NRs (b) and plexcitonic NPs (c) under all polarizations contributing to the longitudinal mode (blue) and to the transversal mode (green) normalized by the nanorod surface area. Black arrows indicate the laser excitation wavelengths at 532 nm and 633 nm. The red arrow points to the transversal excitonic resonance at 574 nm. The dielectric properties of TDBC were considered as a Lorentzian oscillator with a strength of 0.13.

colloidal dispersion. It is crucial therefore to consider the contributions from all polarizations. We start with the polarization exciting the longitudinal mode of the plasmonic nanorods. Figure 2b shows the extinction of a bare Au@Ag NR for linearly polarized light, with polarization either parallel (longitudinal) or perpendicular (transversal) to the NR long axis. As expected, the longitudinal mode exhibits highly localized hotspots at the NR corners, with the maximum electric field enhancement occurring at the NP/water interface (Figure S8a, Supporting Information). A similar spatial distribution is obtained for both 532 nm and 633 nm excitation wavelengths. However, the maximum SERS enhancement factor is approximately one order of magnitude higher for 633 nm than 532 nm (Figure S8b,c, Supporting Information), the opposite trend compared to what was observed experimentally for the plexcitonic NRs. In the case of plexcitonic NRs, the simulated extinction demonstrates the anticipated strong coupling between the longitudinal plasmon resonance and the excitonic transition of TDBC. This coupling gives rise to upper and lower plexcitonic resonances at 555 nm and 604 nm, respectively (Figure 2c). The calculated SERS enhancement factor at 532 nm (**Figure 3**a,g), reveals that the electric field is confined within the TDBC shell, whereas at 633 nm (Figure 3b,g) the field is attenuated within the TDBC shell, obtaining the maximum field enhancement at the TDBC/water interface. We thus propose that confinement of the field within the TDBC shell (at 532 nm) leads to an enhancement of light-matter interactions between the near electric field and the molecular vibrations, ensuring a high SERS signal from the entire layer of TDBC molecules, which are strongly coupled to the plasmonic NP. However, when comparing the calculated enhancement factor in the TDBC shell for both laser excitation wavelengths, the SERS EF for 532 nm is only twice for 633 nm (7×10^3 for 532 nm versus 3×10^3 for 633 nm) for the longitudinal mode.

As mentioned above, our experimental conditions demand that the contribution of all polarizations be considered, including transversal polarizations. Therefore, it is crucial to consider the contributions of all polarizations. The calculated extinction spectra in Figure 2b reveal three transversal resonances below 500 nm for plexcitonic NRs, similar to those in bare Au@Ag NRs. However, an additional resonance at 574 nm is observed. This resonance has been previously predicted for plexcitonic NPs with organic shells, modeled with large oscillator strengths ($\approx f = 0.3$) in spherical core-shell plasmonic nanoparticles.[36] This resonance is associated to the low refractive index of TDBC achieving negative values of the real part of the permittivity within this specific wavelength range.[26,33] Given the proximity of the 532 nm laser wavelength to this excitonic resonance, we analyze the spatial distribution of the electric field to the fourth power for the two possible transversal polarizations at 532 nm (Figure 3c,e) and 633 nm (Figure 3d,f). At 532 nm, the field is strongly confined within the TDBC shell, whereas at 633 nm, the field is damped within the TDBC shell, with the maximum intensity occurring at the TDBC/water interface. Numerically, when considering transversal polarization aligned with the long-axis of the rod (Figure 3c,d), the SERS enhancement factor at 532 nm is 35 times higher than that at 633 nm. Similarly, when considering transversal polarization aligned with the short-axis of the rod (Figure 3e,f), the SERS enhancement factor at 532 nm is 23 times higher than at 633 nm. In summary, when exciting plexcitonic nanorattles at 532 nm, both longitudinal and transverse polarizations contribute significantly to enhancing the Raman signal. However, at 633 nm only the longitudinal contribution is significant. In addition, for plexcitonic nanorattles we observe an opposite trend to that for bare plasmonic NRs, resulting in higher SERS enhancements at shorter wavelengths than the excitonic resonance, resulting in multiband SERS encoded tags.

We would like to remark that the differences in the distribution of the electric field between 532 nm and 633 nm are also observed between the plexcitonic modes at 555 nm and 604 nm. For the upper plexcitonic mode at 555 nm, the electric field is trapped within the TDBC shell, like what happens for 532 nm

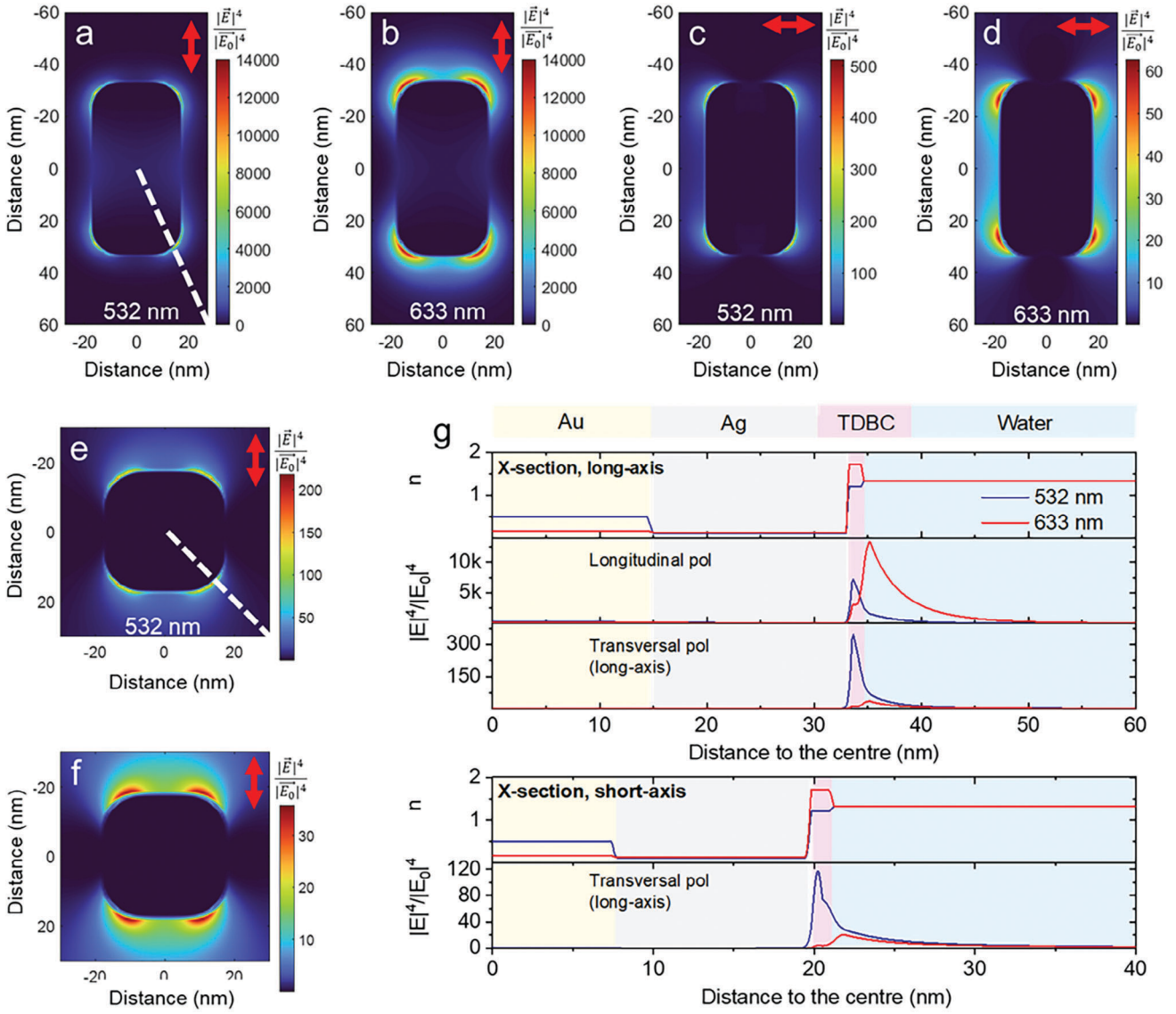

Figure 3. a–f) Calculated spatial distribution of the electric field enhancement to the fourth power in an X-section crossing at the center of a plexcitonic Au@Ag NR in the XZ plane, for polarizations parallel (longitudinal, a and b) and perpendicular (transversal, c and d) to the long axis, and in a plane perpendicular to the long axis (XY plane, e,f), under 532 nm and 633 nm irradiation, as indicated. In all cases, light travels toward the plane. The red double arrows indicate the direction of vibration of the linear polarization. g) Refractive index and SERS enhancement in a line from the center to a corner of the plexcitonic Au@Ag NR in the XZ plane for longitudinal and transversal polarizations (upper panel, dotted white line in Figure 3a), and in the XY plane and for transversal polarization (lower panel, dotted white line in Figure 3e), under 532 nm (blue), and 633 nm (red) irradiation. Areas in yellow indicate the region for the Au core, grey for the silver shell, pink for the TDBC shell, and blue for water.

(Figure S9a,g, Supporting Information). Conversely, for the lower plexcitonic mode at 604 nm, the electric field is attenuated within the TDBC shell, achieving the maximum intensity at TDBC/water interface, similar to 633 nm (Figure S9b,g, Supporting Information). As a result, the SERS enhancement factor is 60 times higher for 555 nm than for 604 excitation wavelength. Additionally, in this case, the excitonic resonance observed at 574 nm for transversal polarization contributes significantly to the Raman enhancement being twice that for 555 nm (Figure S9e–g, Supporting Information). Consequently, to design optimized SERS-encoded plexcitonic NPs it is crucial to tune the upper plexcitonic mode and the transversal excitonic resonance, to match the Raman excitation wavelength.

Considering the previous results, we tested the SERS performance of our plexcitonic nanorattles, using both the 532 and 633 nm laser lines (**Figure 4**). SERS spectra from colloidal dispersions were recorded at decreasing nanorattle concentrations until no significant signal was observed (Figure 4a,b). Next, we calculated the limit of detection (LOD) by plotting the SERS intensity at 1200 cm^{-1} as a function of NP concentration (Figure 4c,d) and applying a linear regression in the analyzed concentration range: 0.3 – 7853.3 fM (1.8×10^5 – 4.7×10^9 NP mL^{-1}) for 532 nm

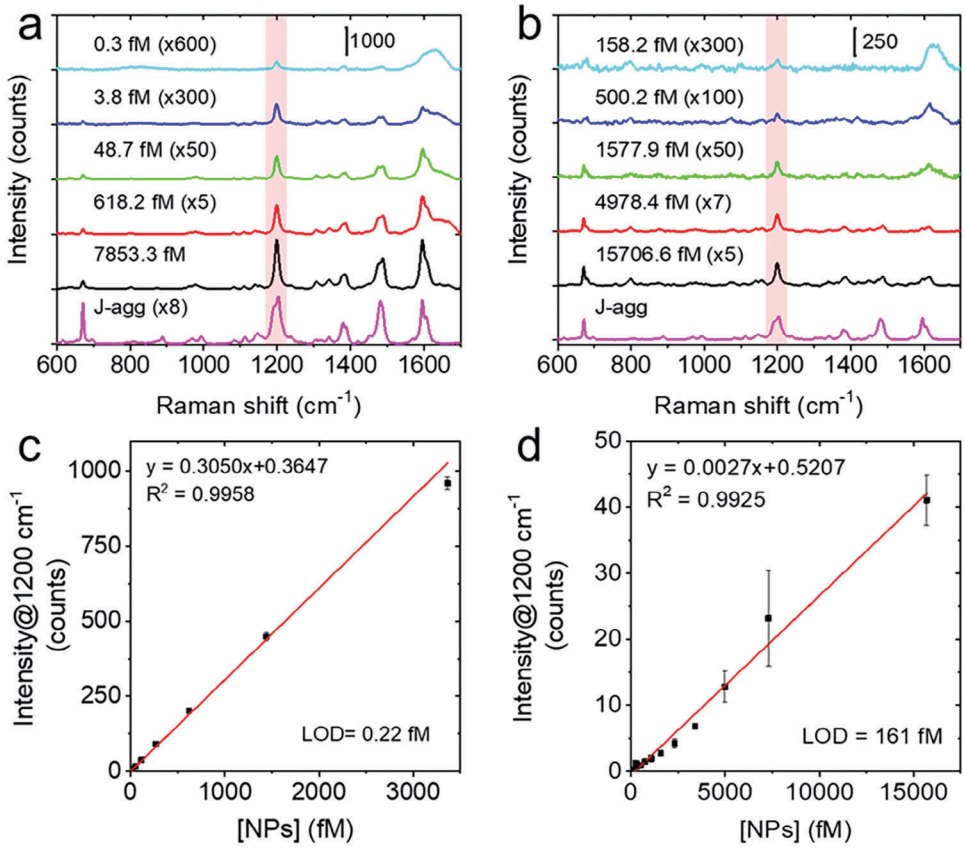

Figure 4. a,b) SERS spectra of colloidal dispersions of plexcitonic nanorattles at different concentrations (as indicated) for 532 nm (a) and 633 nm (b) laser lines. The Raman spectrum of TDBC at each wavelength is included for comparison. Both SERS and Raman spectra were normalized by laser power, acquisition time, and number of accumulations. c,d) SERS intensity of the 1200 cm^{-1} peak, as a function of nanorattle concentration for 532 (c) and 633 nm (d) laser lines.

and 158.2 – 15 706.6 fM (9.6×10^6 – 9.5×10^9 NP mL^{-1}) for the 633 nm. The calculated LOD for each case was found to be 0.22 and 161 fM (1.4×10^5 and 9×10^7 NP mL^{-1}), for 532 nm and 633 nm irradiation, respectively. Although the LOD value obtained for 633 nm is similar to previous reports,[37–40] in the case of 532 nm irradiation, we were able to detect a reliable SERS signal down to concentrations of 0.3 fM (≈10^5 NP mL^{-1}), which is two orders of magnitude lower than those for previously reported SERS tags.[37–40]

To further demonstrate the potential performance of plexcitonic nanorattles as SERS tags, we measured SERS spectra at the single NP level.[41,42] We first acquired 250 SERS spectra from colloidal dispersions of plexcitonic nanorattles with concentrations of 11.2 fM and 1.3 fM, using a 532 nm laser line, 10 s accumulation time, and a 60× water immersion objective (**Figure** 5a–c).[41] Considering a probed volume (V_p) of ≈30 pL, the nanorattle concentration per V_p was estimated as 0.2 and 0.02 for both samples. The minimum signal detected from the SERS-tag dispersion (hereafter threshold limit) was estimated as three times the standard variation in the mean background signal, i.e., 18 counts (see Figure S10, Supporting Information and Experimental Section). Figure 5a–c shows SERS spectra, band intensity at 1200 cm^{-1} and statistical analysis of 240 measurements acquired in time sequence, corresponding to samples with 0.2 and 0.02 NPs/V_p. In the case of the sample with 0.2 NPs/V_p, all SERS spectra show a signal at 1200 cm^{-1} above the threshold limit (Figure 5a,b, top), and the frequency of the normalized SERS signal can be fitted to a Gaussian distribution (Figure 5c, top). For the case of 0.02 NPs/V_p, 70% of the spectra meet the threshold criterion (Figure 5b, bottom) and the statistical analysis shows an intensity distribution that can be fitted to four Gaussian curves, consistent with a Poisson distribution (Figure 5c, bottom). This behavior reflects the probability of finding 0, 1, 2, or 3 NPs inside the probe volume, thereby evidencing the detection of a single particle[41,42] and, therefore, the high SERS efficiency of the plexcitonic nanorattles in colloidal dispersion.

Additionally, to estimate the potential use of plexcitonic nanorattles for quantitative SERS imaging, the average SERS intensity per NP in a given area was determined by means of a recently reported protocol with an associated App (SERSTEM),[27] which allows a statistical correlation of TEM images with SERS maps. A representative example of the procedure for overlapping optical and TEM images is presented in Figure S11 (Supporting Information). Figure 5d shows the analyzed TEM images, depicting in blue the submaps containing points whose SERS spectra statistically matched the reference spectrum (Figure S12, Supporting Information) and in red the position of plexcitonic NPs

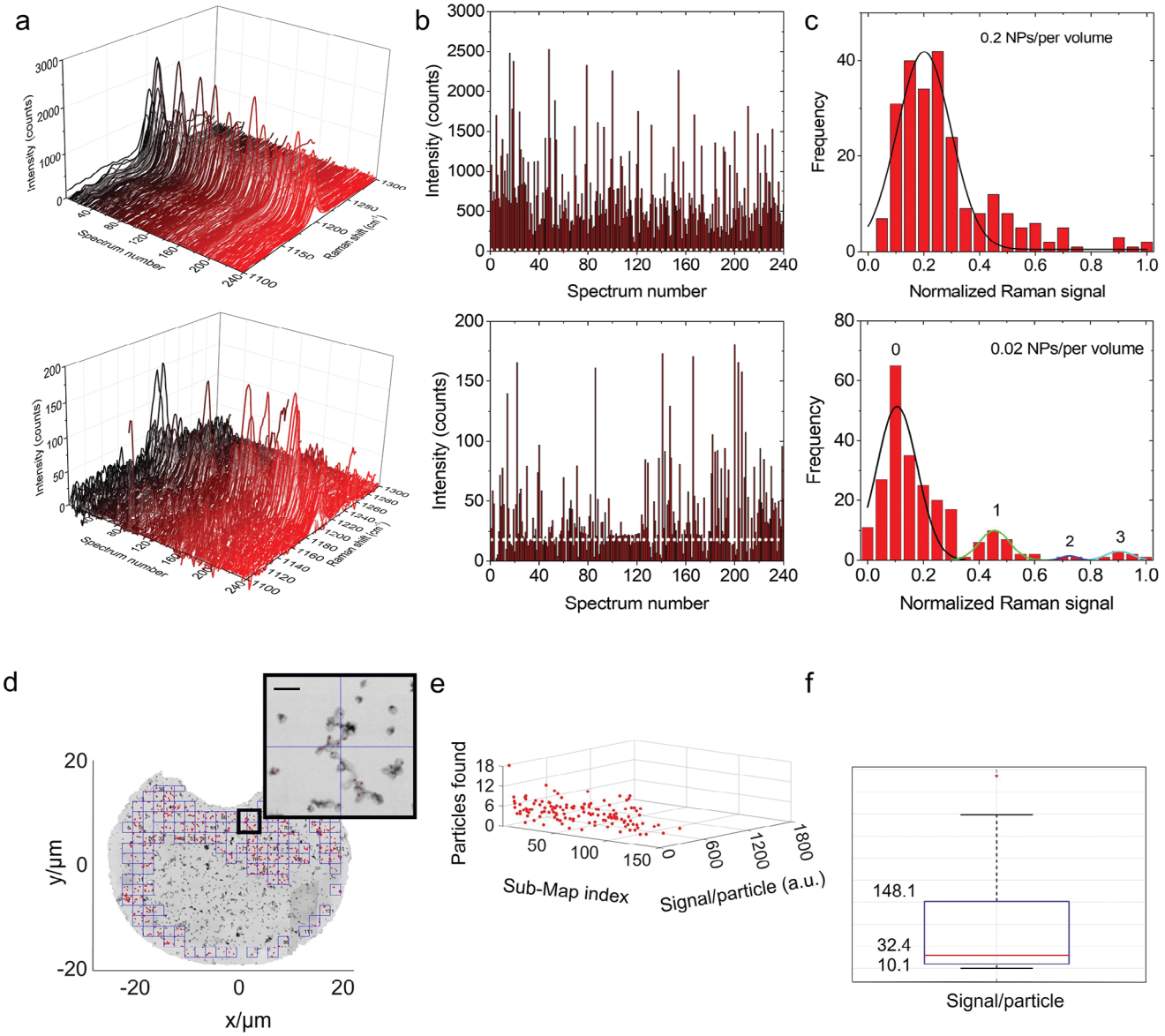

Figure 5. Single-NP detection of plexcitonic nanorattles. a–c) Stacked SERS spectra (a), SERS intensity at 1200 cm^{-1} (b), and statistical distribution of 240 spectra (c), for samples with plexcitonic nanorattle concentrations of 11.2 fM (top) and 1.3 fM (bottom), corresponding to 0.2 and 0.02 NP per probe volume, respectively. In (b) the threshold limit is indicated by dotted lines and black arrows. Solid curves in (c) are Gaussian fittings. All SERS measurements were recorded with a 532 nm laser line at 22.3 mW power, a 15× objective, 10 s acquisition time, and 1 accumulation. d–f) SERSTEM analysis: d) TEM image of the analyzed area showing the different submaps (blue grid). In each submap, we depicted in red the position of plexcitonic nanorattles with an area ranging from 5 to 300 pixels. Scale bar is 1 µm. e) Values of SERS signal per NP at 1200 cm^{-1} considering the number of NPs found in each submap when overlapping the TEM images and the SERS mappings. f) Plot of the average of the SERS signal per NP evidenced the 25% and 75% percentiles of the median value.

with an area between 5 and 300 pixels (minimum to consider an individual particle and maximum to neglect aggregates of particles that can difficult the particle counting). Interestingly, we were able to make a direct comparison of the TEM image and representative spectra from the SERS mapping (Figure S13, Supporting Information). The Feret diameters shown in Figure S14 (Supporting Information) were used to assign the minimum and maximum pixel particle parameters. We additionally represented in a Scatter plot (Figure 5e) the SERS intensity per plexcitonic nanorattle at 1200 cm^{-1} (under 532 nm laser irradiation), corresponding to the points analyzed in each submap considering the 25% and 75% percentiles of the median value (Figure 5d). The signal per particle was found to have a mean value of 32.4 counts, with 50% of the values oscillating between 10 and 148 counts. Within these constraints, 120 spectra and 747 NPs were considered and the number of plexcitonic nanoparticles contributing to each spectrum resulted to be 5.2 ± 3.3, as shown in Figure S15 (Supporting Information). Compared with the previously reported data,[27] the plexcitonic nanorattles reported here show higher SERS efficiency.

3. Conclusions

In summary, we have studied in detail light-matter interactions for plexcitonic nanorattles based on J-aggregates of the cyanine dye TDBC, deposited on plasmonic NPs encapsulated by a hollow silica shell (Au@Ag@mSiO_2). The nanorattle structure facilitated the adsorption of J-aggregates onto the metal NPs surface, while providing high colloidal stability, even in polar organic solvents. Electromagnetic simulations showed that electromagnetic field is strongly enhanced within the J-aggregate layer, at wavelengths close to the upper polariton, but damped toward the J-aggregate/water interface at the lower polariton. This non-wavelength-symmetric response is due to the strong dispersive properties of the J-aggregate shell, achieving low refractive index values that allow confining the light in the J-aggregate shell at all polarizations with no need of strong coupling with a plasmon resonance. These findings were corroborated by SERS spectroscopy showing a high efficiency for the plexcitonic nanorattles under both 633 nm and 532 nm laser illumination. In the first case, we were able to detect meaningful SERS signals from plexcitonic nanorattles in aqueous dispersion down to concentrations similar to previously reported SERS tags. However, for the 532 nm laser line, when the electric field is strongly confined in the J-aggregate layer, we obtained an experimental LOD of 0.3 fM ($\approx 10^5$ NPs mL^{-1}), i.e., two orders of magnitude improvement over previous reports. In addition, a change in the statistical distribution of SERS signals from Gaussian to Poisson distribution, as the concentration of plexcitonic nanorattles decreases, demonstrates a detection sensitivity at the single-NP level. Estimation of the average SERS intensity per plexcitonic nanorattle in the dry state, using the recently reported SERSTEM app, suggests that plexcitonic nanorattles may be the most efficient SERS tag evaluated to date when excited with 532 nm laser.

These findings demonstrate that plexcitonic nanorattles can be exploited as highly efficient SERS-Tags, especially at the wavelength range where the organic layer reaches near-zero index values confining completely the field in the organic shell layer. Further studies are required to further boost the SERS efficiency of plexcitonic nanorattles, e.g. by matching the Raman excitation with the upper polariton branch of longitudinal plexcitonic resonance and the excitonic resonance in the transversal polarization. Therefore, plexcitonic nanorattles may open a new avenue toward ultrasensitive biosensing and bioimaging platform as superbright and highly stable optical labels.

4. Experimental Section

Materials: 5,6-dichloro-2-[[5,6-dichloro-1-ethyl-3-(4-sulfobutyl)-benzimidazol-2-ylidene]-propenyl]−1-ethyl-3-(4-sulfobutyl)-benzimidazolium hydroxyde) (TDBC, 98%) was bought from Few Chemicals. Cetyltrimethylammonium bromide (CTAB, 98%), cetyltrimethylammonium chloride (CTAC, 25% wt. solution), sodium borohydride ($NaBH_4$, 99%), gold (III) chloride trihydrate ($HAuCl_4{\cdot}3H_2O$, 99.9%), silver nitrate ($AgNO_3$, 99%), L-ascorbic acid (≥ 99%), 2-methylimidazole (2-MeIM, 99%), zinc nitrate hexahydrate ($Zn(NO_3)_2{\cdot}6H_2O$, 99%), methanol, ethanol, tetraethyl orthosilicate (TEOS, 98%), hydrochloric acid (HCl, 37%), sodium chloride (NaCl, ≥ 99%) were purchased from Merck (Sigma-Aldrich). Milli-Q water was used in all experiments.

Synthesis of Au Nanorods: Au NRs were synthetized by previously reported a seeded growth methodology.[43] Gold seeds were prepared by the addition of 460 µL of $NaBH_4$ (0.01 M, in NaOH 0.01 M) to 10 mL of an aqueous solution containing 0.5 mM $HAuCl_4$ and 0.1 M CTAB under stirring. The brownish seed solution was aged at 27 °C for 1 h before use. A growth solution was prepared by addition to 10 mL of 0.5 mM $HAuCl_4$ (in CTAB 0.1 M aqueous solution) HCl (180 µL, 1 M), $AgNO_3$ (120 µL, 0.01 M) and ascorbic acid (80 µL, 0.1 M), in this order. This mixture was hand stirred after the addition of each reagent until the solution became clear and quickly add 48 µL of the seed solution. The final mixture was left undisturbed overnight at 27 °C. The Au NRs formed were centrifuged (7000 rpm, 10 min) and the pellet was washed twice with 80 mM CTAC and finally redispersed in 10 mL of 80 mM CTAC. The final Au NR concentration of 0.49 mM (1.07×10^{12} NPs mL^{-1}) was calculated considering that an extinction value of 1.2 at 400 nm corresponds to an Au° concentration of 0.5 mM.[44]

Synthesis of Au@Ag NRs: Au@Ag NRs were synthesized as previously reported.[45] 10 mL of Au NRs (0.068 mM) was diluted in 40 mL of 80 mM CTAC. After that, ascorbic acid (3.5 mL, 0.1 M) and $AgNO_3$ (3.5 mL, 0.01 M) were added, and the solution was left in an oven at 60 °C for 3 h. The formed Au@Ag NRs were cooled down to room temperature and the NPs were washed twice (8000 rpm, 15 min) with 10 mL of Milli-Q water adjusting the final concentration of CTAC to 0.6 mM. A final Au@Ag NR concentration of 1.48×10^{11} NPs mL^{-1} was estimated by considering no losses during the washing steps, as indicated by UV-vis spectra of the supernatants.

Synthesis of Au@Ag@ZIF-8 NPs: Au@Ag@ZIF-8 NPs were synthesized as previously reported.[46] Briefly, under stirring in a vial, CTAC (144 µL, 1 mM) was added to 2-MeIM (1 mL, 1.32 M) and stirred for 5 min. After that, $Zn(NO_3)_2{\cdot}6H_2O$ (1 mL, 24 mM) and 1 mL of the Au@Ag core-shell NRs ($1.48{\times}10^{11}$ NPs mL^{-1}) were added, stirred for 5 min and, left undisturbed for 3 h. Finally, the Au@Ag@ZIF-8 were washed once with 10 mL of methanol (5000 rpm, 10 min) and redispersed in 3.14 mL of methanol. A final Au@Ag@ZIF-8 concentration of $2.97{\times}10^{10}$ NPs mL^{-1} was estimated by considering no losses during the washing steps.

Synthesis of Au@Ag@mSiO_2 Nanorattles: Au@Ag@mSiO_2 nanorattles were prepared following a sacrificial template approach.[30] First, Au@Ag@ZIF-8 NPs ($2.97{\times}10^{10}$ NPs mL^{-1}) were coated with a thin mesoporous silica layer. Briefly, 3.14 mL of Au@Ag@ZIF-8 NPs was centrifuged (5000 rpm, 5 min) and the supernatant was discarded. The pellet was left at 60 °C in an oven and once dried, redispersed in a mixture of CTAB (16 mL, 1.5 mM) and 2-MeIM (100 µL, 1.32 M). Then, three aliquots of TEOS (25 µL, 10% v/v in ethanol) were added in 1 h intervals under stirring, and after the third addition, the mixture was stirred overnight. The resulting Au@Ag@ ZIF-8@mSiO_2 NPs were washed twice with 10 mL of ethanol (6000 rpm, 10 min) and finally redispersed in 5 mL of Milli-Q water. Second, for the etching of the ZIF-8 used as template, HCl (3 mL, 0.06 M) was added to the NPs and the mixture was sonicated for 15 min. After that, the Au@Ag@mSiO_2 nanorattles were centrifuged (6000 rpm, 5 min) and washed trice with ethanol. Finally, the nanorattles were redispersed in 2 mL of ethanol. A final Au@Ag@mSiO_2 NP concentration of $1.89{\times}10^{10}$ NPs mL^{-1} was estimated by considering no losses during the washing steps.

Synthesis of Plexcitonic Au@Ag@mSiO_2 Nanorattles: 500 µL of Au@Ag@mSiO_2 nanorattles was mixed with TDBC dissolved in ethanol (500 µL, 50 µM) and left under stirring in a rotator stirrer at 20 rpm for 20 min. Subsequently, the NPs were washed (6000 rpm, 5 min) once in water and twice in ethanol to remove the excess TDBC. Finally, the NPs were dispersed in 500 µL of ethanol.

Synthesis of Plexcitonic Au@Ag NRs: 150 µL of the Au@Ag NRs ($1.48{\times}10^{11}$ NPs mL^{-1}) prepared as described above was centrifuged (7500 rpm, 5 min) and redispersed in 500 µL of CTAB 10 mM. In a vial, the Au@Ag NRs were mixed with 4.9 mL of Mill-Q water and CTAB (600 µL, 0.1 M) under stirring for 2 min. Then, four additions of TDBC (75 µL, 0.5 mM in ethanol) were added in 10 min intervals. After that, the NPs were washed (7500 rpm, 10 min) trice in 10 mM CTAB to remove the excess TDBC. Finally, the NPs were redispersed in 1 mL of 10 mM CTAB. The zeta potential of the Au@Ag NRs was measured to vary from +60 mV to +40 mV, upon TDBC deposition.

Electromagnetic Simulations: FDTD simulations were carried out using commercial Lumerical Ansys software. The extinction, absorption, and scattering cross-sections were estimated by the combination of total-field scattered-field linearly polarized and a cross-section analysis group. All data were normalized by the NP surface to obtain the cross-section efficiency per particle. The unpolarized results were obtained by averaging the cross sections for all possible linear polarizations. Maps of the local electromagnetic field intensity were obtained using field monitors crossing by the center of the particle.

Characterization: Optical characterization was performed in an Agilent 8453 UV-visible spectrophotometer with quartz cuvettes with a 5 mm optical path. Transmission electron microscopy (TEM) images were collected in a JEOL JEM 1010 operating at 100 kV voltage. For the TEM grids, 3–4 drops of 10 µL were poured on a carbon-coated copper grid over filter paper and dried at room temperature before the observation.

SERS Experiments: Measurements were conducted in a micro-Renishaw InVia Reflex system composed of a confocal microscope, high resolution diffraction grating (1200 grooves cm^{-1}) with an additional pass filter and, a 2D-CCD camera. In the limit of detection experiments, the excitation wavelength of the lasers used for the experiments where 532 and 633 nm laser excitation line and a 15× lens objective was used. All spectra were acquired and treated using WiRE Software v. 4.3 (Renishaw, UK) applying the following steps: cosmic ray removal, noise filter, and baseline subtraction.

In the case of the single particle experiments, plexcitonic nanorattles in ethanol were centrifuged (6000 rpm, 5 min) and redispersed in the same volume of Milli-Q water. Then the sample was deposited inside a handmade PDMS well dish and covered with a cover slide. In this case, the laser excitation was 532 nm and the objective used was a 60× water immersion. Thus, 250 SERS spectra were acquired in time sequence for 0.2 and 0.02 NPs per volume samples. For the statistical analysis the spectra with the 10 highest intensities at 1200 cm^{-1} were discarded. The minimum signal detected coming from SERS tag dispersion or threshold limit was estimated as three times the standard variation in the mean background signal obtained after acquiring 250 spectra in a highly diluted sample of plexcitonic nanorattles.

SERSTEM Analysis: Evaluation of SERS performance of the plexcitonic nanorattles was accomplished according to a statistical analysis of correlative SERS and transmission electron microscopy (TEM) imaging reported by E. Lenzi et al.[27] The application can be downloaded at http://wwwdisc.chimica.unipd.it/nanostructures.optics/SERSTEM.html.

For that, 5 µL aliquot of plexcitonic colloidal dispersion in ethanol ($1{,}5 \times 10^{10}$ NPs mL^{-1} to ensure an adequate SERS signal-to-noise ratio preventing NPs aggregation to perform the counting) was deposited onto a hydrophilized TEM grid labeled with recognizable characters for the correlation of SERS mapping and TEM imaging area. To prevent NP reshaping or damage to Raman active molecules under the electron beam during TEM observations, Raman mapping was first executed. The area inside an asymmetric letter such as Q was chosen for SERS mapping since it presented a flatter morphology and prevented loss of focus.

SERS Mapping: SERS measurements were collected with a confocal Raman microscope (Renishaw inVia) equipped with 1024×512 CCD detectors, using a 532 nm laser excitation source and a 1800 l mm^{-1} diffraction grating. SERS maps were captured in static mode (scattered wavenumber centered on 1200 cm^{-1}) using a 50× long working distance objective (numerical aperture, NA = 0.5; Leica Microsystems, Wetzlar, Germany) with 0.5 s integration time, at 2.43 mW laser power. The map (48×38 μm^2) was acquired with a resolution of 1 µm in x- and y-axis. No re-mapping was performed in the same area to check the photobleaching of the nanorattles. Nevertheless, it is considered that the irradiation time (0.5 s) was short enough to prevent photobleaching. SERS reference spectra were collected from a 5 µL drop of the plexcitonic nanorattles (25 130 mM) on top of a quartz slide using a 50× long working distance objective (NA = 0.5; Leica Microsystems, Wetzlar, Germany) in expanded scan mode with an integration time of 1 s, at a laser power of 23.27 mW and one accumulative scan.

TEM Imaging: A 200-mesh copper–carbon film London finder grid for electron microscopy was treated by glow discharge to hydrophilize the surface and obtain a homogeneous spreading of the particles. After 7 min in vacuum (10^{-1}), negative polarity is applied with a coating current of 30 mA for 2 min and 30 s. Immediately after, a 5 µL drop of nanorattles at 1.5×10^{10} NPs mL^{-1} is deposited which is allowed to dry in air. TEM images were acquired with a JEOL JEM-1400PLUS transmission electron microscope operating at 120 kV. To image the area, with an extension larger than the field of view at 5000× magnification, 212 consecutive images were taken (with an overlap between each other of ≈40% of the total image. Post-reconstruction of the whole image was done through a dedicated tool available in Fiji, Microscopy Image Stitching Tool (MIST).[47]

For the analysis of the images via SERSTEM app the TEM image must be accurately superimposed on the optical image, which is connected by spatial coordinates with the SERS map (Figure S12, Supporting Information). Several parameters should be adjusted in the program such as the gray limit value (GLV) Raman shift and *p* and *b* values threshold, which depends on the TEM image contrast and on SERS measurement signal-to-noise ratio. The Min-Max pixel particle and map subdivision should be optimized for each sample analysis as well in order to exclude undesired aggregates. All the established parameters are reported in Table S1 (Supporting Information).

Supporting Information

Supporting Information is available from the Wiley Online Library or from the author.

Acknowledgements

S.N.-S., J.P.-J, C.E.-V. and I.P.-S. acknowledge financial support from MCIN/AEI/10.13039/501100011033 (Grant No. PID2019-108954RB-I00 and PRE2020-096163) and the European Innovation Council (Horizon 2020 Project: 965018—BIOCELLPHE). L.M.L.-M. acknowledges funding from the European Research Council (ERC AdG #787510). D.J.deA. acknowledges financial support from MCIN/AEI/10.13039/501100011033 (Grant No. PID2019-108854RA-I00). P.P.-V. acknowledges an FPU Fellowship from the Spanish Ministerio de Ciencia e Innovación (PRE2020-094237). S.N.-S. acknowledges the Portuguese Foundation for Science and Technology for the individual contract 2022.03164. CEECIND and F.J. Díaz-Otero and D. Álvarez-Outerelo for free access to their computational facilities. CACTI is acknowledged for using TEM facilities. [Correction added on 4 December 2023, after first online publication: CRUE-CISUG funding statement has been added.]

Funding for open access by the Universidade de Vigo/CISUG.

Conflict of Interest

The authors declare no conflict of interest.

Data Availability Statement

The data that support the findings of this study are available at ZENODO, doi: 10.5281/zenodo.10065723

Keywords

J-aggregate, nanoplasmonics, plexcitonic nanoparticles, SERS tags, strong coupling, surface-enhanced Raman scattering spectroscopy

Received: July 18, 2023
Revised: November 2, 2023
Published online: November 27, 2023

[1] Y. Xia, D. J. Campbell, *J. Chem. Educ.* **2007**, *84*, 91.
[2] H. Leng, B. Szychowski, M.-C. Daniel, M. Pelton, *Nat. Commun.* **2018**, *9*, 4012.
[3] V. Krivenkov, P. Samokhvalov, I. Nabiev, Y. P. Rakovich, *J. Phys. Chem. C* **2021**, *125*, 1972.
[4] D. Melnikau, A. A. Govyadinov, A. Sánchez-Iglesias, M. Grzelczak, I. R. Nabiev, L. M. Liz-Marzán, Y. P. Rakovich, *J. Phys. Chem. Lett.* **2019**, *10*, 6137.
[5] K. Liang, J. Guo, F. Wu, Y. Huang, L. Yu, *J. Phys. Chem. C* **2021**, *125*, 17303.
[6] E. Cao, W. Lin, M. Sun, W. Liang, Y. Song, *Nanophotonics* **2018**, *7*, 145.
[7] A. P. Manuel, A. Kirkey, N. Mahdi, K. Shankar, *J. Mater. Chem. C* **2019**, *7*, 1821.
[8] D. G. Baranov, M. Wersäll, J. Cuadra, T. J. Antosiewicz, T. Shegai, *ACS Photonics* **2018**, *5*, 24.
[9] P. Törmä, W. L. Barnes, *Rep. Progr. Phys.* **2015**, *78*, 013901.
[10] Q. Zhao, W.-J. Zhou, Y.-H. Deng, Y.-Q. Zheng, Z.-H. Shi, L. Kee Ang, Z.-K. Zhou, L. Wu, *J. Phys. D Appl. Phys.* **2022**, *55*, 203002.
[11] T. Brixner, R. Hildner, J. Köhler, C. Lambert, F. Würthner, *Adv. Energy. Mater.* **2017**, *7*, 1700236.
[12] C. M. Walters, C. Pao, B. P. Gagnon, C. R. Zamecnik, G. C. Walker, *Adv. Mater.* **2018**, *30*, 1705381.
[13] N. Peruffo, F. Mancin, E. Collini, *J. Phys. Chem. C* **2021**, *125*, 19897.
[14] J. L. Bricks, Y. L. Slominskii, I. D. Panas, A. P. Demchenko, *Meth. Appl. Fluoresc.* **2018**, *6*, 012001.
[15] F. Würthner, T. E. Kaiser, C. R. Saha-Möller, *Angew. Chem., Int. Ed.* **2011**, *50*, 3376.
[16] J. Langer, D. Jimenez De Aberasturi, J. Aizpurua, R. A. Alvarez-Puebla, B. Auguié, J. J. Baumberg, G. C. Bazan, S. E. J. Bell, A. Boisen, A. G. Brolo, J. Choo, D. Cialla-May, V. Deckert, L. Fabris, K. Faulds, F. J. García De Abajo, R. Goodacre, D. Graham, A. J. Haes, C. L. Haynes, C. Huck, T. Itoh, M. Käll, J. Kneipp, N. A. Kotov, H. Kuang, E. C. Le Ru, H. K. Lee, J.-F. Li, X. Y. Ling, et al., *ACS Nano* **2020**, *14*, 28.
[17] E. C. Le Ru, P. G. Etchegoin, *Chem. Phys. Lett.* **2006**, *423*, 63.
[18] D. García-Lojo, S. Gómez-Graña, V. F. Martín, D. M. Solís, J. M. Taboada, J. Pérez-Juste, I. Pastoriza-Santos, *ACS Appl. Mater. Interfaces* **2020**, *12*, 46557.
[19] D. Jimenez De Aberasturi, A. B. Serrano-Montes, J. Langer, M. Henriksen-Lacey, W. J. Parak, L. M. Liz-Marzán, *Chem. Mater.* **2016**, *28*, 6779.
[20] T. Hendel, V. Krivenkov, A. Sánchez-Iglesias, M. Grzelczak, Y. P. Rakovich, *Nanoscale* **2020**, *12*, 16875.
[21] B. Munkhbat, M. Wersäll, D. G. Baranov, T. J. Antosiewicz, T. Shegai, *Sci. Adv.* **2023**, *4*, eaas9552.
[22] A. Shalabney, J. George, H. Hiura, J. A. Hutchison, C. Genet, P. Hellwig, T. W. Ebbesen, *Angew. Chem., Int. Ed.* **2015**, *54*, 7971.
[23] J. Galego, F. J. Garcia-Vidal, J. Feist, *Nat. Commun.* **2016**, *7*, 13841.
[24] L. Sun, Z. Li, J. He, P. Wang, *Nanophotonics* **2019**, *8*, 1835.
[25] S. T. Holder, C. Estévez-Varela, I. Pastoriza-Santos, M. Lopez-Garcia, R. Oulton, S. Núñez-Sánchez, *Nanophotonics* **2023**, *12*, 307.
[26] M. A. Castillo, C. Estévez-Varela, W. P. Wardley, R. Serna, I. Pastoriza-Santos, S. Núñez-Sánchez, M. Lopez-Garcia, *Adv. Funct. Mater.* **2022**, *32*, 2113039.
[27] E. Lenzi, L. Litti, D. Jimenez De Aberasturi, M. Henriksen-Lacey, L. M. Liz-Marzán, *J. Raman Spectrosc.* **2021**, *52*, 355.
[28] D. Djoumessi Lekeufack, A. Brioude, A. W. Coleman, P. Miele, J. Bellessa, L. De Zeng, P. Stadelmann, *Appl. Phys. Lett.* **2010**, *96*, 253107.
[29] A. V. Sorokin, I. Y. Ropakova, R. S. Grynyov, M. M. Vilkisky, V. M. Liakh, I. A. Borovoy, S. L. Yefimova, Y. V. Malyukin, *Dyes Pigments* **2018**, *152*, 49.
[30] S. De Marchi, D. García-Lojo, G. Bodelón, J. Pérez-Juste, I. Pastoriza-Santos, *ACS Appl. Mater. Interfaces* **2021**, *13*, 61587.
[31] W. J. Harrison, D. L. Mateer, G. J. T. Tiddy, *J. Phys. Chem.* **1996**, *100*, 2310.
[32] M. J. Gentile, S. Núñez-Sánchez, W. L. Barnes, *Nano Lett.* **2014**, *14*, 2339.
[33] T. J. Antosiewicz, S. P. Apell, T. Shegai, *ACS Photonics* **2014**, *1*, 454.
[34] R. Thomas, A. Thomas, S. Pullanchery, L. Joseph, S. M. Somasundaran, R. S. Swathi, S. K. Gray, K. G. Thomas, *ACS Nano* **2018**, *12*, 402.
[35] D. M. Coles, A. J. H. M. Meijer, W. C. Tsoi, M. D. B. Charlton, J.-S. Kim, D. G. Lidzey, *J. Phys. Chem. A* **2010**, *114*, 11920.
[36] T. J. Antosiewicz, S. P. Apell, T. Shegai, *ACS Photonics* **2014**, *1*, 454.
[37] J.-M. Nam, J.-W. Oh, H. Lee, Y. D. Suh, *Acc. Chem. Res.* **2016**, *49*, 2746.
[38] X. Zhuo, M. Henriksen-Lacey, D. Jimenez De Aberasturi, A. Sánchez-Iglesias, L. M. Liz-Marzán, *Chem. Mater.* **2020**, *32*, 5879.
[39] C. Fernández-López, L. Polavarapu, D. M. Solís, J. M. Taboada, F. Obelleiro, R. Contreras-Cáceres, I. Pastoriza-Santos, J. Pérez-Juste, *ACS Appl. Mater. Interfaces* **2015**, *7*, 12530.
[40] S. Rodal-Cedeira, A. Vázquez-Arias, G. Bodelón, A. Skorikov, S. Núñez-Sánchez, A. Laporta, L. Polavarapu, S. Bals, L. M. Liz-Marzán, J. Pérez-Juste, I. Pastoriza-Santos, *ACS Nano* **2020**, *14*, 14655.
[41] Y. Zhang, Y. Gu, J. He, B. D. Thackray, J. Ye, *Nat. Commun.* **2019**, *10*, 3905.
[42] K. Kneipp, Y. Wang, H. Kneipp, L. T. Perelman, I. Itzkan, R. R. Dasari, M. S. Feld, *Phys. Rev. Lett.* **1997**, *78*, 1667.
[43] B. Nikoobakht, M. A. El-Sayed, *Chem. Mater.* **2003**, *15*, 1957.
[44] L. Scarabelli, A. Sánchez-Iglesias, J. Pérez-Juste, L. M. Liz-Marzán, *J. Phys. Chem. Lett.* **2015**, *6*, 4270.
[45] S. Gómez-Graña, B. Goris, T. Altantzis, C. Fernández-López, E. Carbó-Argibay, A. Guerrero-Martínez, N. Almora-Barrios, N. López, I. Pastoriza-Santos, J. Pérez-Juste, S. Bals, G. Van Tendeloo, L. M. Liz-Marzán, *J. Phys. Chem. Lett.* **2013**, *4*, 2209.
[46] G. Zheng, S. De Marchi, V. López-Puente, K. Sentosun, L. Polavarapu, I. Pérez-Juste, E. H. Hill, S. Bals, L. M. Liz-Marzán, I. Pastoriza-Santos, J. Pérez-Juste, *Small* **2016**, *12*, 3935.
[47] J. Schindelin, I. Arganda-Carreras, E. Frise, V. Kaynig, M. Longair, T. Pietzsch, S. Preibisch, C. Rueden, S. Saalfeld, B. Schmid, J.-Y. Tinevez, D. J. White, V. Hartenstein, K. Eliceiri, P. Tomancak, A. Cardona, *Nat. Methods* **2012**, *9*, 676.